

Inverse-scattering separable NN potential constrained to phase-shift data up to 2.5 GeV. I.- Uncoupled states

H. F. Arellano^{1,2*} and N. A. Adriaola¹

¹Department of Physics - FCFM, University of Chile, Av. Blanco
Encalada 2008, Santiago, RM 8370449, Chile.

²CEA, DAM, DIF, F-91297 ArpaJon, France.

*Corresponding author(s). E-mail(s): arellano@df.uchile.cl;

Abstract

We introduce a new method to construct, within inverse-scattering theory, an energy-independent separable potential capable of reproducing exactly both phase shift and absorption over a predefined energy range. The approach relies on the construction of non-overlapping multi-rank separable potentials, whose form factors are obtained by solving linear equations on intervals where the \mathbf{K} matrix does not have zeros. Applications are made to nucleon-nucleon (NN) interactions constrained to the SAID-SP07 phase-shift analysis up to 2.5 GeV lab energy. The inversion potentials are channel dependent with rank dictated by the number of zeros of the \mathbf{K} matrix, reproducing the data up to a selected upper momentum. The account for absorption yields complex separable form factors, resulting in a non-Hermitian potential. Applications are restricted to NN spin-uncoupled states considering a Schrödinger-like wave equation with minimal relativity. Its extension to spin-coupled states and relativistic kernels are discussed.

1 Introduction

The concept of two-body potentials to represent the interaction between nucleons has proven to be a powerful tool for *ab-initio* and microscopic studies of nuclear many-body phenomena such as nuclear reactions, nuclear structure and nuclear matter equation-of-state. Soon after Hideki Yukawa introduced his one-pion-exchange theory [1] to describe the nucleon-nucleon (NN) interaction, sustained progress has been made over

the years towards building meson-exchange potential models [2–4], and more recently, chiral effective field theory interactions with pionic degrees of freedom [5–11].

In all these constructions a limited set of parameters are adjusted to provide optimal fits to NN scattering data and static properties of the deuteron, the only two-nucleon bound state in free space. A common feature of these realistic potential models is that they are designed to account for phase-shift data at nucleon beam energies of up to about 300 MeV. In the context of chiral perturbation theory, the most advanced developments go up to order of six, becoming limited to lab energies of 0.5 GeV at the most [11, 12], where inelasticities are small. Thus, the resulting potentials turn out to be Hermitian, consistent with the fact that no loss of flux takes place in NN collisions at these energies. At higher energies these realistic potentials become unsuitable as their implied scattering amplitude constitute extrapolations of the model, together with their inability to account for the loss of flux above the pion production threshold. From a phenomenological stand point, such limitations in realistic potentials can be corrected by adding an energy- and state-dependent separable term with predefined form factors [13, 14].

In this paper we introduce a novel framework to obtain a separable representation for the NN interaction constrained to known scattering amplitude as function of the energy. The method we propose enables an exact reproduction of the on-shell NN scattering data within an energy domain up to an upper limit. There are no limitations regarding the presence of inelasticities above meson production threshold. The resulting form factors are model- and energy-independent. In order to keep the focus on the framework, its implementation and scope, we limit this article to spin-uncoupled NN states.

Separable representations of the NN interaction have the advantage over their fundamental counterparts, in that the number of operations needed to evaluate certain matrix elements in few- and many-body systems diminishes drastically. This sole element may dictate whether a computationally intensive calculation becomes feasible or not under current floating-point operations per second (FLOPS) speeds. However, one has to keep in mind that separable interactions are artifacts designed to model specific aspects of the interaction.

Among the earliest developments, within inverse scattering theory, is the possibility of constructing nonlocal separable interactions extracting their form factors from phase-shift data [15–17]. The particularity of this approach is that a rank-one separable interaction can be obtained through inverse scattering with the only constrain given by the elastic scattering amplitude. The method can be extended to cases where the phase shift crosses the zero axis within the range of construction. In Ref. [18] this inverse-scattering approach was implemented for nucleon beam energies of up to 1.6 GeV, neglecting inelasticities [18]. Along a different line, in Ref. [19] a rank- N separable potential was developed for the Paris potential [3]. The construction considers up to four Yukawa-type form factors, providing optimal fits to NN phase-shift data up to 300 MeV. In Ref. [20], the authors have constructed a complex separable potential to describe the 3SD_1 state fitted to data up to 1.1 GeV. More recently, in Ref. [21] the authors present an algebraic method to solve inverse scattering based on Marchenko theory, obtaining an energy-independent separable potential in the 1S_0 channel up to 3 GeV.

This article is organized as follows. In Sec. 2 we outline the theoretical framework where we construct an inverse-scattering multi-rank separable potential from on-shell scattering amplitude. We also discuss features exhibited by the NN phase-shift data relevant for this work. This is followed with actual applications, where we present solutions to channels of interest, paying attention on the structure of the solutions and the role of absorption in the data. In Sec. 3 we summarize the main findings of this work and discuss its scope.

2 Theoretical framework

Let us consider two nucleons interacting by means of potential \hat{V} . The equation of motion for the interacting pair in the center-of-momentum reference frame (c.m.) is taken as [22, 23]

$$\left(\hat{p}^2 + m\hat{V}\right)\Psi = k^2\Psi, \quad (1)$$

where m is the nucleon mass and k is the relativistic c.m. relative momentum for asymptotic states. This approach has been broadly adopted by various groups in the construction of high precision realistic NN potentials [2-4, 24].

The scattering \hat{T} matrix associated to Eq. (1) reads

$$\hat{T}(z) = \hat{V} + \hat{V}\hat{G}_0(z)\hat{T}(z), \quad (2)$$

with $\hat{G}_0(z) = m/(z - \hat{p}^2)$, the free propagator and z an energy parameter. For outgoing scattering states we express $z = \omega + i\eta$, with $\omega > 0$, and η a positive infinitesimal. With this notation we denote $G_0^{(+)}(\omega) = G_0(\omega + i\eta)$.

Considering a rank-one separable potential given by

$$\hat{V} = |a\rangle\lambda\langle\tilde{a}|, \quad (3)$$

with λ a sign constant, its corresponding scattering T matrix becomes

$$\hat{T}(\omega) = \frac{|a\rangle\lambda\langle\tilde{a}|}{1 - \lambda\langle\tilde{a}|G_0^{(+)}(\omega)|a\rangle}. \quad (4)$$

This equation establishes a link between the scattering matrix \hat{T} , and the form factors $|a\rangle$ and $\langle\tilde{a}|$. To proceed further we introduce the following ansatz for the form factors projected in momentum space

$$\langle p|a\rangle = \langle\tilde{a}|p\rangle = \frac{f(p)}{\sqrt{mp}}, \quad (5)$$

where $f(p)$ is a function to be determined from the data. As we shall see, in the presence of absorption this function becomes complex. Projecting Eq. (4) in momentum space

with $\langle k|$ on the left, $|k\rangle$ on the right and taking $\omega = k^2$, we obtain

$$t(k) \left[1 - \frac{2}{\pi} \int_0^\infty \frac{\lambda f^2(p) p dp}{k^2 + i\epsilon - p^2} \right] = \lambda f^2(k). \quad (6)$$

Here $t(k) \equiv mk \langle k | \hat{T}(k^2) | k \rangle$, denotes the on-shell scattering matrix element. What turns out interesting from this result is that for a given set of data defined by $t(k)$, there is a unique solution for $\varphi(k) \equiv \lambda f^2(k)$. This feature is evidenced after discretizing the above integral in the momentum variable p , resulting in a linear equation for $\varphi(p)$.

To make contact with the scattering data we adopt the parametrization of the scattering amplitude given in Refs. [25, 26], which for uncoupled channels is summarized by the \bar{K} matrix expressed as

$$\bar{K}(k) = \tan \delta(k) + i \tan^2[\rho(k)]. \quad (7)$$

Here δ and ρ denote phase shift and absorption, respectively. This matrix is related to t through

$$t(k) = -\frac{\bar{K}(k)}{1 - i\bar{K}(k)}. \quad (8)$$

With these definitions Eq. (6) reduces to the following linear equation for φ

$$\bar{K}(k) \left[1 - \frac{2}{\pi} \mathcal{P} \int_0^\infty \frac{\varphi(p) p dp}{k^2 - p^2} \right] = -\varphi(k), \quad (9)$$

where \mathcal{P} denotes principal-value integral. This equation summarizes the interrelation between the square of the separable form factor, $\varphi(k)$, and the on-shell scattering data contained in \bar{K} . In the absence of inelasticities, when $\rho=0$, φ becomes real. From the above equation we note that there is a one-to-one correspondence between zeros of \bar{K} and those of φ , meaning that φ keeps the same sign on intervals where \bar{K} does not vanish. Thus, to extract the form factor $f = \sqrt{\lambda\varphi}$, we define $\lambda = \text{Sgn}\{\varphi\}$.

A necessary condition for the existence of a solution to Eq. (9) is that for increasing k , $\varphi(k)$ decreases at least as $\sim k^{-\nu}$, with $\nu > 0$. Since the scattering data is given over a finite energy range, there is no feasible way to verify this condition. A way to circumvent this limitation, without compromising the ability to reproduce the data within its domain of definition, is by introducing a smooth cutoff to suppress high momentum contribution in the \mathcal{P} integral. Techniques of similar nature are adopted in the context of renormalization group models [27].

In order to unfold φ from Eq. (9) we apply a smooth ultraviolet (UV) cutoff to $\bar{K}(k)$, namely

$$\bar{K}(k) \rightarrow \hat{\Theta}(k_c - k) \bar{K}(k), \quad (10)$$

where

$$\hat{\Theta}(x) = \begin{cases} 1, & \text{if } x \leq 0; \\ e^{-x^2/d^2}, & \text{if } x > 0; \end{cases} \quad (11)$$

with d its diffuseness. Note that this regulator and its derivatives are continuous in the whole range. Its advantage is that it does not alter the integrand below k_c , but it cuts

off smoothly the high momentum components of \bar{K} . The reason we apply the cutoff to \bar{K} and not to the scattering amplitude is to preserve unitarity of the solutions when $\rho=0$. In this work we use $d=0.05 \text{ fm}^{-1}$, throughout.

2.1 Phase-shift data

We base the present study on the SAID-SP07 solution of the phase-shift analysis [28] available at the INS Data Analysis Center of The George Washington University [29], for np data up to 2.5 GeV lab energy. In the case of NN uncoupled states the data is represented by means of the phase shifts δ and absorption ρ over a broad range of laboratory energies E , with $k = \sqrt{mE/2}$, the relativistic relative momentum. Given that in our approach the nature of inverse-scattering solutions depend on features of the scattering amplitude as function of the energy, we briefly examine them in the case of NN uncoupled channels.

In Table 1 we list all NN uncoupled states considered in this work. Underlined states denote states with phase-shift crossing the zero axis at some energy below 2.5 GeV, property that requires specific considerations when there is no absorption. States with nonzero ρ are shown with gray background. As observed, the only elastic state with nonzero phase-shifts are 1F_3 , 3G_4 , 1H_5 , 3I_6 and 1J_7 .

ST	Allowed NN states							
0 1	<u>1S_0</u>	.	<u>1D_2</u>	.	<u>1G_4</u>	.	<u>1I_6</u>	.
0 0	.	<u>1P_1</u>	.	1F_3	.	1H_5	.	1J_7
1 0	.	.	<u>3D_2</u>	.	3G_4	.	3I_6	.
1 1	<u>3P_0</u>	3P_1	.	<u>3F_3</u>	.	3H_5	.	<u>3J_7</u>

Table 1 NN uncoupled states considered in this work. States with zeros in the phase-shift appear underlined. Those with absorption above pion threshold are shown on gray background. Features based on SAID SP07 phase-shift analysis of Ref. [29].

In Fig. 1 we plot the phase-shift and absorption for spin-zero states as functions of nucleon beam energy. Panels (a) and (c) show the absorption parameter ρ as a function of the nucleon beam energy E_{Lab} , while panels (b) and (d) show the phase-shift δ . Frames (a) and (b) correspond to isovector ($T=1$) channels, whereas frames (c) and (d) correspond to isoscalar ($T=0$) ones. Short red segments indicate energies at which δ crosses the zero axis in the 1S_0 and 1D_2 channels. As observed, all isovector channels exhibit absorption above the pion production threshold ($E_{Lab} \gtrsim 290 \text{ MeV}$). Below 1 GeV the absorption is more pronounced for the 1D_2 state. We also notice that the phase-shifts δ vanishes near 290 MeV in the case of 1S_0 state, and two times (around 890 and 1900 MeV) in the case of channel 1D_2 . For the isoscalar channel, only 1P_1 state exhibits absorption, with zero phase-shift around 1660 and 2240 MeV.

In Fig. 2 we show plots for δ and ρ for $S=1$, spin-uncoupled states. Frames (a) and (b) correspond to isoscalar channels, whereas frames (c) and (d) correspond to

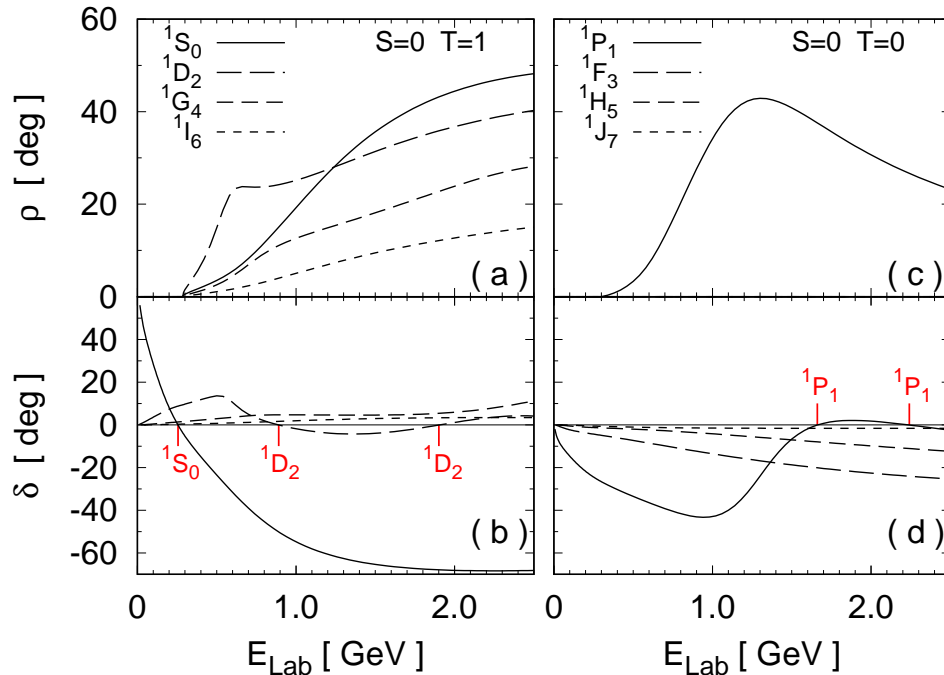


Fig. 1 Absorption parameter ρ [(a), (c)] and phase-shift δ [(b), (d)] as functions of the nucleon beam energy E_{Lab} for spin-0 NN states with $J \leq 7$. Frames (a) and (b) correspond to $T=1$ channels, whereas frames (c) and (d) correspond to $T=0$. Vertical red segments indicate zeros in the phase-shift.

isovector ones. In the case of isoscalar states we observe that 3D_2 , 3G_4 and 3I_4 channels are elastic, while only 3D_2 exhibits zero phase-shift around 1115 MeV. This scenario contrasts with the isovector channels, where absorption is present in all states. Below 1 GeV, the absorption is stronger in the 3P_0 and 3P_1 states. Additionally, the phase-shift in channel 3P_0 vanishes around 200 MeV while for channel 3F_3 it crosses twice the zero axis near 640 MeV.

2.2 Solutions

Based on the SP07 phase-shift analysis discussed in the preceding section, we proceed to calculate the form factors $f(k)$ solutions of Eq. (6), making use of on-shell scattering data summarized by the matrix $T(k)$. To solve this equation we discretize the momentum p over a uniform array of N elements, $p \rightarrow p_j = jh$, with $h = p_{max}/N$, the momentum step length. Here $p_{max} = k_c + \Delta$, with $\Delta \approx 2 \text{ fm}^{-1}$. The resulting equation for $\varphi(p_j) = \varphi_j$ takes the matrix form

$$\sum_{j=1}^N M_{ij} \varphi_j = b_i, \quad (12)$$

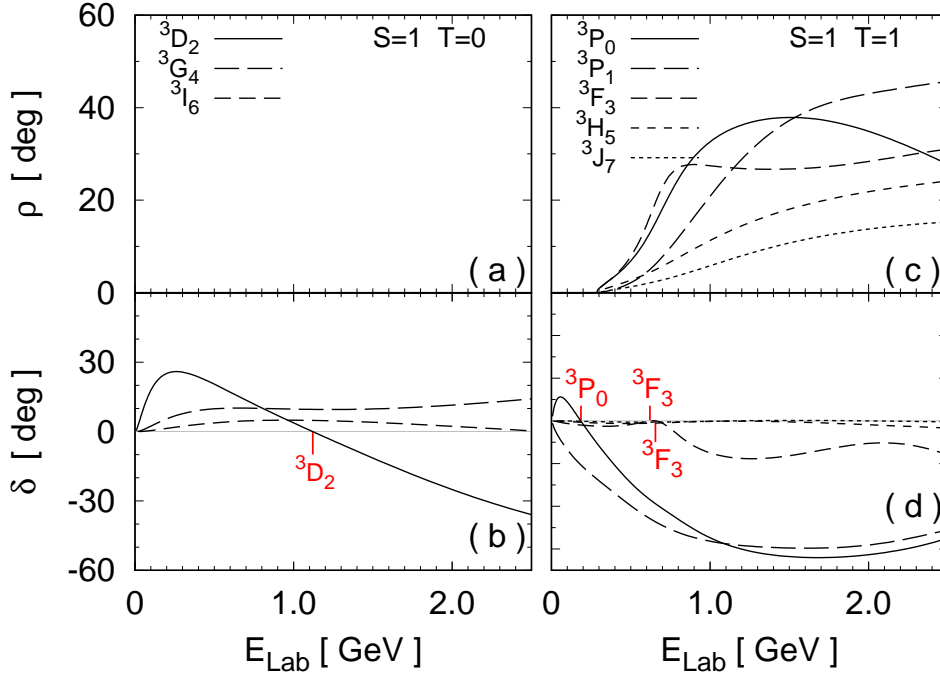


Fig. 2 The same as Fig. 1 but for spin-1 uncoupled NN states.

where \mathbb{M} is a square matrix built from on-shell data and trapezoidal quadrature coefficients. The same holds for array \mathbb{b} . Regarding the low-momentum extrapolation of phase-shift data we consider two cases: *a*) $S=0$ waves, where we use the low- k effective-range expansion; and *b*) $S \geq 1$ waves, where we apply a power fit of the type $\delta(k) = ak^p$. Once φ is obtained by direct matrix inversion, we proceed to take its square root to obtain the form factor, $f(k) = \sqrt{\lambda\varphi(k)}$, with λ the sign of the solution.

The procedure outlined above is applied to the 1F_3 channel, featuring no absorption and nonzero phase shift in the whole energy range. To illustrate the role of the UV cutoff, we consider four different values: $k_c = 2.5, 3.5, 4.5$ and 5.5 fm^{-1} . The corresponding results for $f(k)$ are shown in Fig. 3, where labels in parenthesis indicate k_c in fm^{-1} units. These energy-independent solutions define rank-one separable potentials reproducing exactly the phase-shift $\delta(k)$ up to $k = k_c$. This is illustrated in Fig. 4, where we plot the on-shell t matrix as given by the phase-shift as function of k , the relativistic relative momentum in the c.m. Open circles and squares denote $\text{Re}\{t\}$ and $\text{Im}\{t\}$, respectively. The calculated t matrix for the separable potential is obtained from Eq. (4). As observed, the agreement between the data and the t matrix from the inverse-scattering form factors is quite good up to $k = k_c$. Above this bound $\text{Re}\{t\}$ and $\text{Im}\{t\}$ fall rapidly due to the regulator.

2.2.1 Solutions for 1S_0 channel.-

Let us now address the 1S_0 channel, featuring a zero in $\delta(k)$ in the energy range. Channels with similar behavior to this one are 1D_2 , 3D_2 , 3P_0 and 3F_3 . In principle we

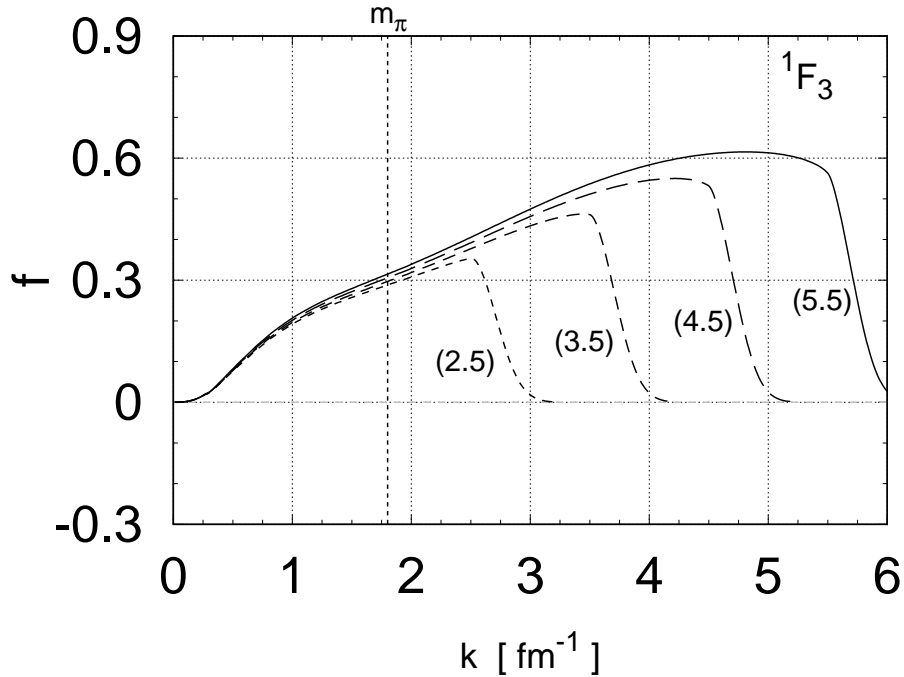


Fig. 3 Calculated form factor $f(k)$ as function of the relative momentum in the case of 1F_3 channel. Solid, long-, medium- and short-dashed curves denote cutoffs of 5.5, 4.5, 3.5 and 2.5 fm^{-1} , respectively.

can also apply Eq. (12) to obtain the corresponding $\varphi(k)$. The resulting solution also exhibits a zero at the point at which δ vanishes. In the particular case when $\rho=0$, this leads to a real and continuous $\varphi(k)$, with a node at $k=k_1$, the zero of the phase-shift. Therefore, the resulting $f(k)$ becomes complex, an scenario we choose to avoid.

The effect of a node in the phase-shift has been addressed by Bolsteri in Ref. [16], proposing the construction of piecewise solutions over intervals where the phase-shift does not have a zero. Following this idea and considering that the phase-shift in channel 1S_0 has a single zero at a given momentum k_1 , we introduce the rank-two interaction

$$\hat{V} = |a_1\rangle\lambda_1\langle\tilde{a}_1| + |a_2\rangle\lambda_2\langle\tilde{a}_2|, \quad (13)$$

with $\lambda_2 = -\lambda_1$. We also define

$$\langle k|a_1\rangle = \langle\tilde{a}_1|k\rangle = \Theta(k_1 - k) \frac{f_1(k)}{\sqrt{mk}}; \quad (14a)$$

$$\langle k|a_2\rangle = \langle\tilde{a}_2|k\rangle = \Theta(k - k_1) \frac{f_2(k)}{\sqrt{mk}}; \quad (14b)$$

where Θ denotes the Heaviside step function while f_1 and f_2 are form factors associated with intervals $[0, k_1]$ and $[k_1, k_{max}]$, respectively. With these definitions we note that $\langle\tilde{a}_1|a_2\rangle = \langle\tilde{a}_2|a_1\rangle = 0$.

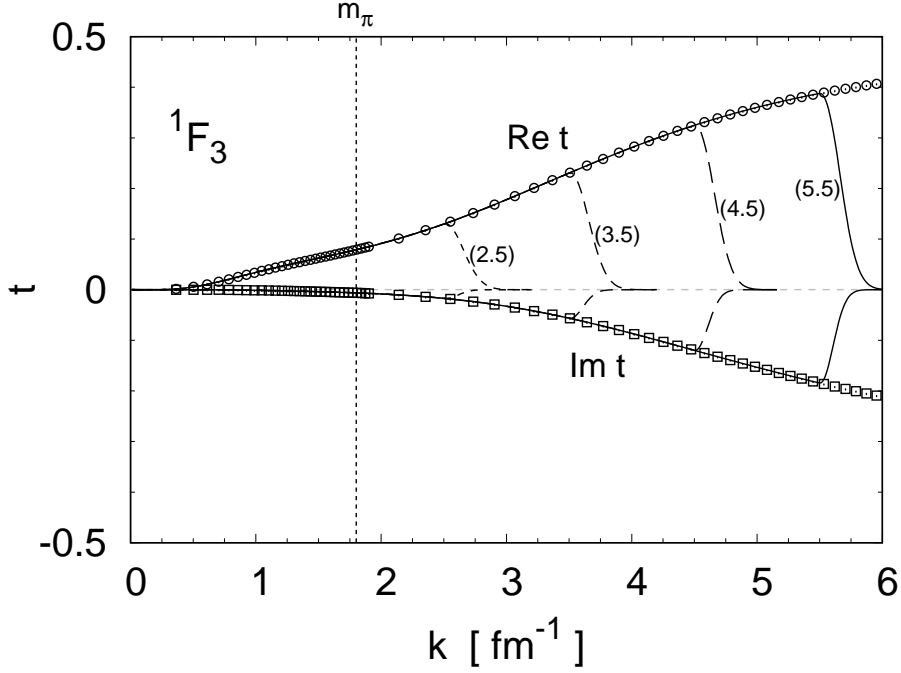


Fig. 4 t matrix as function of the relative momentum for the 1F_3 channel. Circles (squares) denote the real (imaginary) component of t based on the SP07 data. Solid, long-, medium- and short-dashed curves denote t -matrix based on separable solutions with UV cutoffs at 5.5, 4.5, 3.5 and 2.5 fm^{-1} , respectively.

To obtain the equations for $\varphi_1 = f_1^2$, and $\varphi_2 = f_2^2$, the procedure outlined in the Appendix yields

$$\bar{K}(k) \left[1 - \frac{2}{\pi} \mathcal{P} \int_0^{k_1} \frac{\varphi_1(p) p dp}{k^2 - p^2} \right] = -\varphi_1(k); \quad (15a)$$

$$\bar{K}(k) \left[1 - \frac{2}{\pi} \mathcal{P} \int_{k_1}^{\infty} \frac{\varphi_2(p) p dp}{k^2 - p^2} \right] = -\varphi_2(k). \quad (15b)$$

In Eqs. (15a) and (15b) we impose $k \leq k_1$, and $k \geq k_1$, respectively. Thus, the equations for inverse form factors f_1 and f_2 take the form Eq. (12), which are solved independently on each of the two intervals.

In Fig. 5 we plot the calculated form factors f_1 and f_2 as functions of the relative momentum for the 1S_0 channel. Red curves represent results suppressing absorption ($\rho = 0$) while black curves including it ($\rho \neq 0$). In both cases $\lambda_1 = -1$, and $\lambda_2 = +1$. Solid, long-, medium- and short-dashed curves correspond to results with $k_c = 5.5, 4.5, 3.5$ and 2.5 fm^{-1} , respectively. We observe mild differences in $\text{Re}\{f_2\}$ when absorption is considered, being more pronounced when $k_c = 5.5 \text{ fm}^{-1}$. Results for $\text{Im}\{f\}$, taking place for nonzero absorption, have been amplified by a factor of four ($\times 4$). As observed, these weak contributions have negative sign relative to their real counterpart.

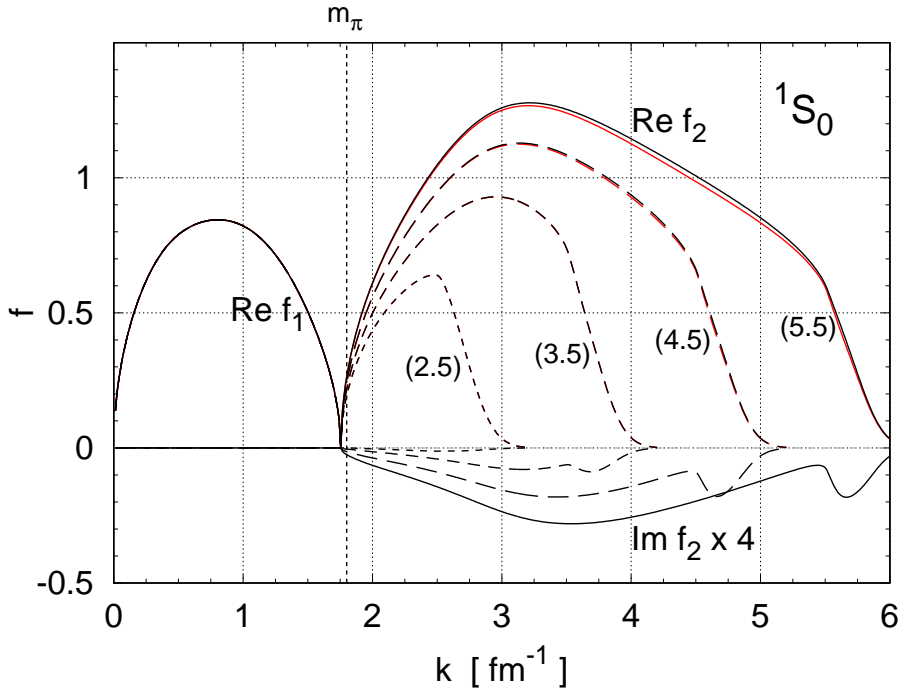


Fig. 5 Calculated form factors f_1 and f_2 as functions of the relative momentum for the 1S_0 channel. Solid, long-, medium- and short-dashed curves denote cutoffs of 5.5, 4.5, 3.5 and 2.5 fm^{-1} , respectively. Solutions with $\rho=0$, are shown in red, while those with $\rho \neq 0$ are shown in black. The imaginary components of f_2 have been amplified by a factor of four.

In Fig. 6 we compare the calculated t matrix obtained from inverse-scattering potentials and the data, including the cases $\rho = 0$, and $\rho \neq 0$. Different curve textures are used for each UV cutoff, adopting the same convention as in Fig. 5. Circles (squares) denote $\text{Re}\{t\}$ ($\text{Im}\{t\}$) from the data. Filled and empty symbols denote inclusion and suppression of absorption, respectively. We observe that the inverse-scattering solutions match the data in the whole k -range, up to their respective UV cutoff.

To visualize the shape of the inversion potential in the kk' plane, Fig. 7 shows a surface plot of $v(k', k) = \langle k' | \hat{V} | k \rangle$ for the rank-2 solution in the 1S_0 channel. For this illustration we suppress absorption by setting $\rho=0$. Here we observe a tile structure formed by two domes on square domains, with nodal lines $k=k_1$, and $k'=k_1$, taking place at the zero of the phase-shift. The convex dome, taking place when k and k' lie below k_1 , is determined by the positive phase-shift in this channel, as seen in panel (b) of Fig. 1. By construction, this energy-independent potential accounts for all phase-shift up to $k=5.5 \text{ fm}^{-1}$, namely 2.5 GeV lab energy.

2.2.2 The case of 1P_1 channel.-

The 1P_1 channel is the only singlet-odd channel with absorption, having also two zeros in the phase-shift. Following our previous discussion, if absorption is omitted, then

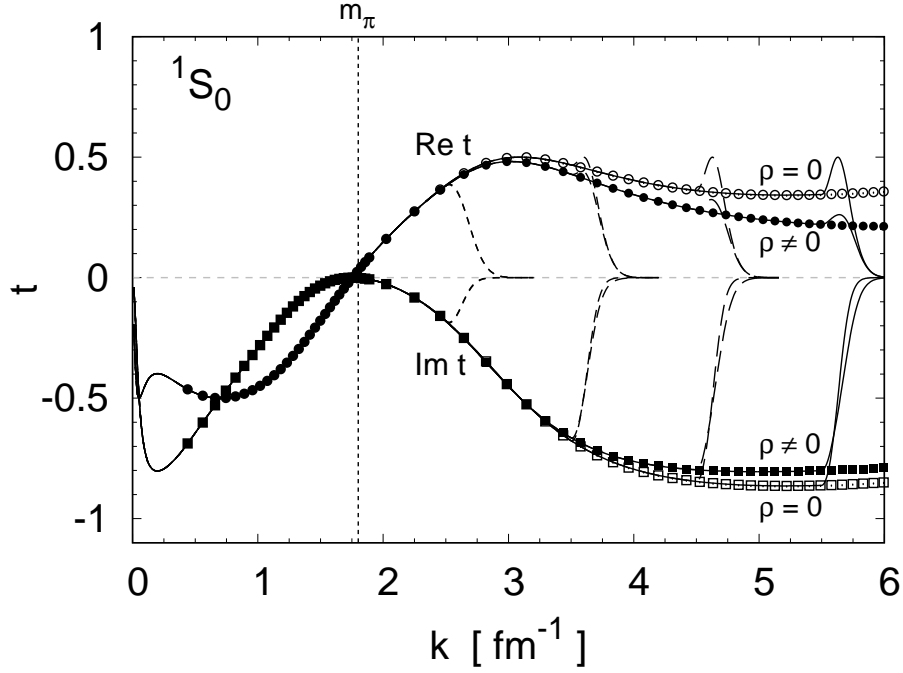


Fig. 6 t matrix as function of the relative momentum for the 1S_0 channel. Circles (squares) denote the real (imaginary) component of t based on the SP07 data. Open (filled) symbols correspond to cases with $\rho=0$ ($\rho \neq 0$). Continuous curves denote t from the separable solutions with different UV cutoffs, adopting the same pattern convention as in Fig. 5.

the separable potential is of rank 3, that is to say

$$\hat{V} = |a_1\rangle\lambda_1\langle\tilde{a}_1| + |a_2\rangle\lambda_2\langle\tilde{a}_2| + |a_3\rangle\lambda_3\langle\tilde{a}_3|, \quad (16)$$

with $\lambda_1 = \lambda_3 = -\lambda_2$. The corresponding form factors are in this case

$$\langle k|a_1\rangle = \langle\tilde{a}_1|k\rangle = \Theta(k_1 - k) \frac{f_1(k)}{\sqrt{mk}}; \quad (17a)$$

$$\langle k|a_2\rangle = \langle\tilde{a}_2|k\rangle = \Theta(k - k_1) \Theta(k_2 - k) \frac{f_2(k)}{\sqrt{mk}}; \quad (17b)$$

$$\langle k|a_3\rangle = \langle\tilde{a}_3|k\rangle = \Theta(k - k_2) \frac{f_3(k)}{\sqrt{mk}}. \quad (17c)$$

Following the Appendix, the associated equations for $\varphi_1 = f_1^2$, $\varphi_2 = f_2^2$ and $\varphi_3 = f_3^2$ become

$$\bar{K}(k) \left[1 - \frac{2}{\pi} \mathcal{P} \int_0^{k_1} \frac{\varphi_1(p) p dp}{k^2 - p^2} \right] = -\varphi_1(k); \quad (18a)$$

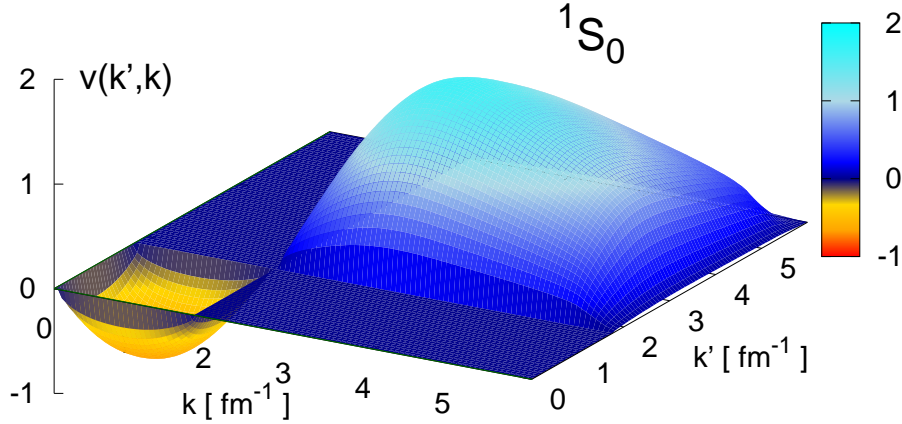


Fig. 7 Surface plot of the rank-2 energy-independent separable potential $v(k', k)$ in the 1S_0 channel, as function of the relative momentum.

$$\bar{K}(k) \left[1 - \frac{2}{\pi} \mathcal{P} \int_{k_1}^{k_2} \frac{\varphi_2(p) p dp}{k^2 - p^2} \right] = -\varphi_2(k); \quad (18b)$$

$$\bar{K}(k) \left[1 - \frac{2}{\pi} \mathcal{P} \int_{k_2}^{\infty} \frac{\varphi_3(p) p dp}{k^2 - p^2} \right] = -\varphi_3(k). \quad (18c)$$

To obtain the solutions φ_1 , φ_2 and φ_3 we follow an analogous procedure to the one applied for the 1S_0 channel.

In Fig. 8 we plot the resulting form factors $f(k)$ for channel 1P_1 as function of the relative momentum k . Red curves denote solutions without absorption ($\rho = 0$), displaying only real solutions. Black curves denote solutions including absorption ($\rho \neq 0$), with $\text{Re}\{f\}$ positive and $\text{Im}\{f\}$ negative. Solid, long-dashed, dashed and short-dashed curves denote solutions with UV cutoff at 5.5, 4.5, 3.5 and 2.5 fm^{-1} , respectively. The vertical blue line correspond to the pion mass.

We observe that all solutions $f(k)$ vanish at the origin while they fall rapidly to zero above their respective k_c . Solid red curves denote the rank-3 solutions (f_1 , f_2 and f_3) without absorption, with $k_c = 5.5 \text{ fm}^{-1}$. This rank arises from the two zeros of the phase-shift, k_1 and k_2 , taking place below k_c . As k_c diminishes to 4.5 fm^{-1} , the rank of the solution decreases to two (red long-dashed curves). For $k_c = 3.5 \text{ fm}^{-1}$ and below, the solution becomes rank-1 (red dashed and short-dashed curves). When absorption is accounted for, $\bar{K}(k)$ does not have zeros in the whole range, leading to rank-1 solutions. These are shown with black curves whose patterns depend on k_c , adopting the same convention as in Fig. 5. Focusing on the two solid curves, we notice that the solution with absorption ($\rho \neq 0$) wraps the rank-3 solutions in red.

The ability of these inversion solutions to reproduce the on-shell data is illustrated in Fig. 9, where we plot the real and imaginary components of the on-shell t matrix as functions of the relative momentum k . Circles (squares) denote $\text{Re}\{t\}$ ($\text{Im}\{t\}$) from the data. Filled and empty symbols denote inclusion and suppression of absorption, respectively. Different curve textures are used for each UV cutoff, adopting the same convention as in Fig. 5. We observe that the inverse-scattering solutions match the

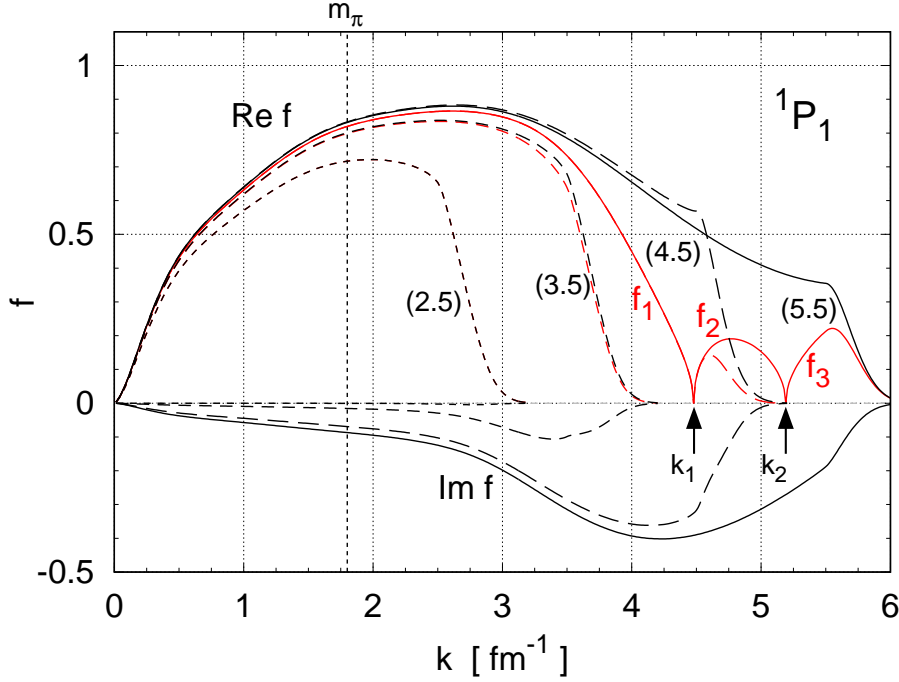


Fig. 8 Calculated form factor $f(k)$ as function of the relative momentum in the case of 1P_1 channel. Black and red curves represent results including and excluding absorption, respectively. Solid, long-, medium- and short-dashed curves denote cutoffs of 5.5, 4.5, 3.5 and 2.5 fm^{-1} , respectively. Labels k_1 and k_2 correspond to zeros of the phase-shift.

data in the whole range of momenta, up to its respective UV cutoff k_c . This level of agreement is replicated to all other states considered in this study.

2.2.3 Global results

We extend the applications described in the previous sub-sections to all states with $J \leq 7$. The UV cutoff is kept equal to 5.5 fm^{-1} throughout. In Fig. 10 we plot the resulting form factors f for all states with $0 \leq J \leq 3$. Black and red curves denote results including and suppressing absorption, respectively. Solid and dashed curves represent $\text{Re}\{f\}$ and $\text{Im}\{t\}$, respectively. The (\pm) signs on the lower left-and-side of each panel denote the sign of λ_1 of the solutions. Panels (a-d) show results for singlet states while panels (e-h) show the ones for triplet states. We note that the role of absorption in the solutions appear most pronounced in channels 1P_1 , 1D_2 and 3F_3 , as differences between red and black curves become more evident.

In Fig. 11 we plot the resulting form factors f for all states with $4 \leq J \leq 7$. The curve colors and patterns follow the same convention as in Fig. 10. Panels (a-d) show results for singlet states while panels (e-h) show the ones for triplet states. In general all solutions follow the same trend as in the cases for $J \leq 3$, with non-negligible absorption in the triplet states 3H_5 and 3J_7 .

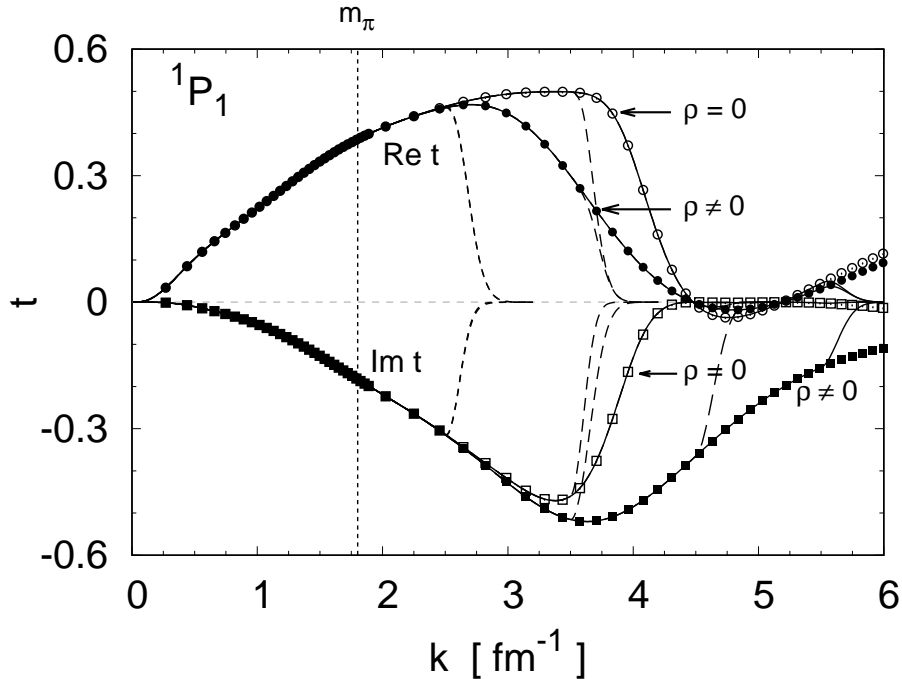


Fig. 9 On-shell t matrix in the 1P_1 channel as function of the relative momentum. Circles (squares) denote $\text{Re}\{t\}$ ($\text{Im}\{t\}$) from the data. Filled and empty symbols denote inclusion and suppression of absorption, respectively. Curve patterns follow the same convention as in Fig. 5

To illustrate the non-Hermitian structure of the potential in the 1D_2 state, in Fig. 12 we show a surface plot of the resulting rank-1 separable potential in the kk' plane. Here $v(k', k) = \lambda f(k')f(k)$, with $\lambda = -1$. The upper and lower surfaces represent the real and imaginary components of the potential, respectively. By observing $\text{Re}\{v\}$ we notice overall attraction followed by strong repulsion at short distances (large k, k'). Similarly, $\text{Im}\{v\}$ exhibits strong absorption at short distances. The actual effect of these features in the NN potential can be investigated in more specific applications, such as nucleon-nucleus scattering [14], an issue of interest but beyond the focus of this work.

3 Summary and conclusions

We have presented a method to construct, within inverse-scattering theory, an energy-independent separable potential capable of reproducing both phase-shift and absorption over a predefined energy range. The approach relies on the construction of non-overlapping multi-rank separable potentials, whose form factors satisfy simple linear equations on intervals where the K matrix does have zeros. The method is applied to NN interactions with scattering data taken from the SAID-SP07 phase-shift analysis with focus on spin-uncoupled states, considering a Schrödinger-like wave equation with minimal relativity. The inversion potentials are channel dependent, of varying

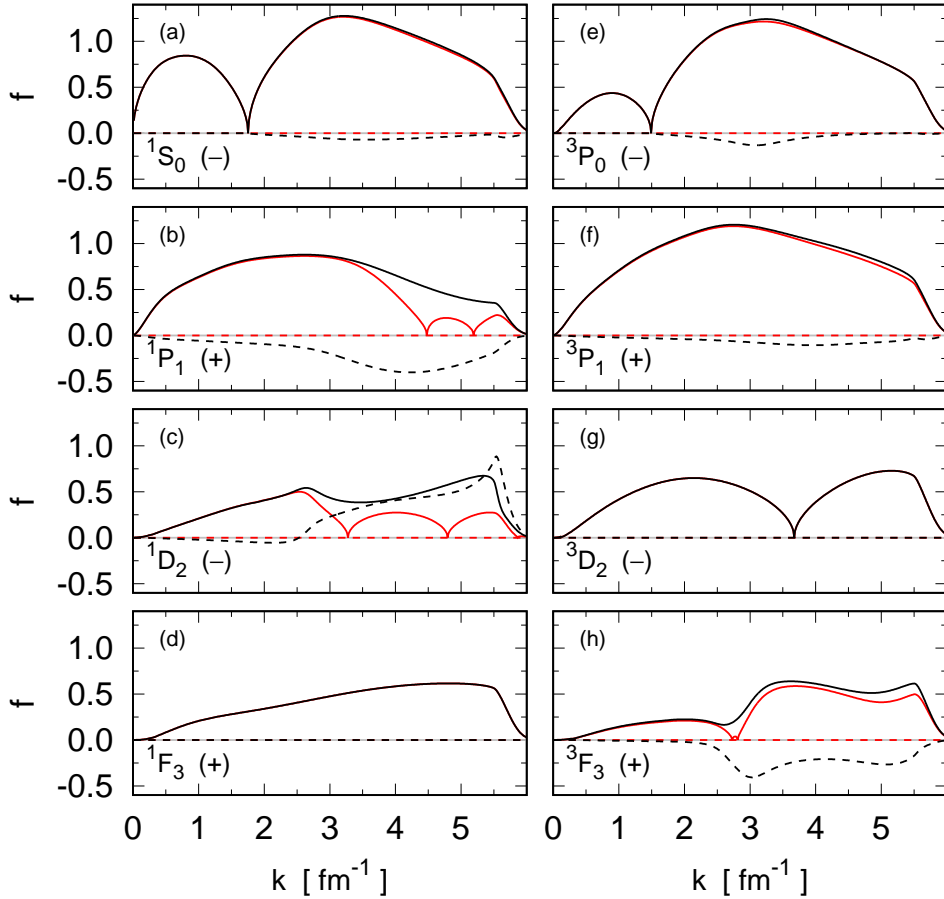


Fig. 10 Calculated form factor $f(k)$ as function of the relative momentum for NN uncoupled states with $J \leq 3$. Solid and dashed curves denote $\text{Re}\{f\}$ and $\text{Im}\{f\}$, respectively. Black (red) curves denote solutions with $\rho \neq 0$ ($\rho = 0$).

rank depending on the number of zeros of the K matrix, reproducing exactly the data up to the selected upper momentum.

The method we have introduced allows for the selective inclusion/exclusion of absorption in the calculation of form factors of the inversion potential. In this respect the framework is broad enough to assess implications of bare NN interactions in domains where loss of flux becomes important, an issue of relevance in near-GeV nucleon-nucleus collisions [14].

Although applications made here have been restricted to Schrödinger-like wave equations, other more general frameworks such as Thompson's relativistic equation [12, 30, 31] can naturally be incorporated. In such a case the evaluation of $\langle \tilde{a} | \hat{G}_0^{(+)}(\omega) | a \rangle$ would involve the energy denominator

$$2(m^2 + \omega)^{1/2} + i\epsilon - 2(m^2 + \hat{p}^2)^{1/2}, \quad (19)$$

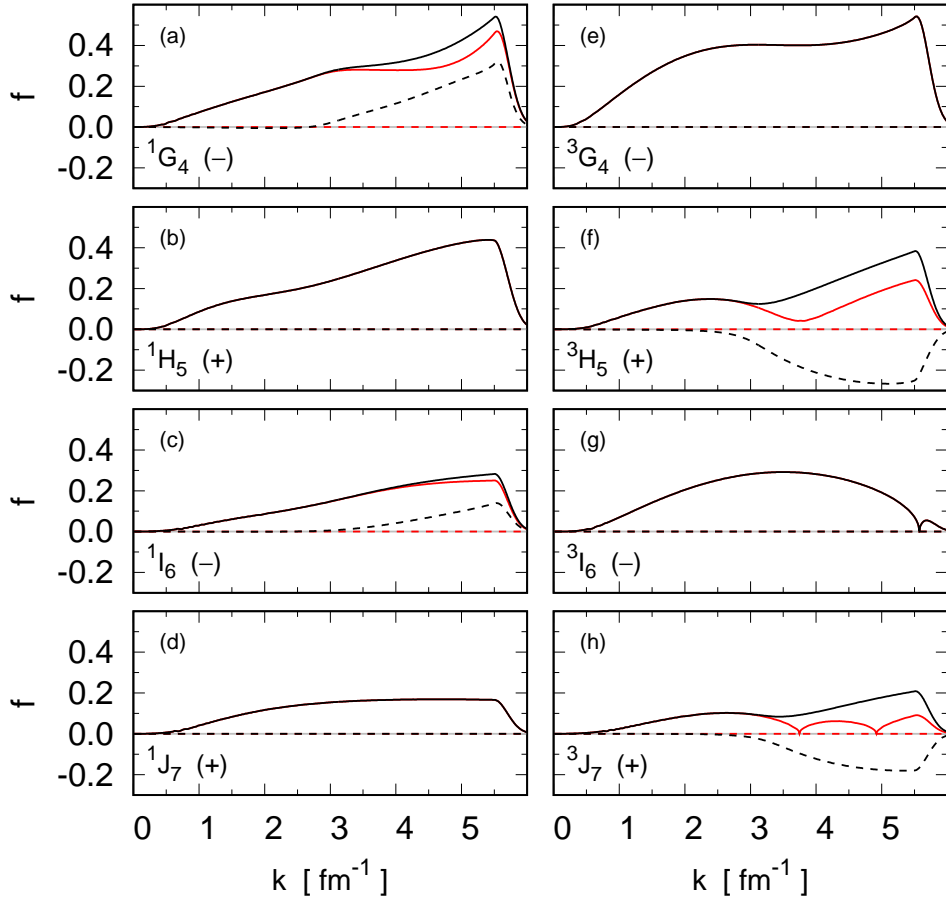


Fig. 11 Calculated form factor $f(k)$ as function of the relative momentum for NN uncoupled states with $4 \leq J \leq 7$. Solid and dashed curves denote $\text{Re}\{f\}$ and $\text{Im}\{f\}$, respectively. Black (red) curves denote solutions with $\rho \neq 0$ ($\rho = 0$).

with $\omega = k^2$. The decay of the associated propagator as a function of the intermediate momenta goes as $\sim 1/p$. Thus, the use of UV cutoffs becomes instrumental for obtaining an equation for φ , over a finite p -array, analogous to that in Eq. (12)

For clarity purposes we have focused this work on laying out the inversion formalism and investigate features of the solutions, considering spin-uncoupled states as given by the NN scattering data. Its extension to coupled states requires specific considerations, whose results will be reported elsewhere. The basic idea in this case is to consider Eq. (2) for coupled states, resulting in

$$\hat{T}(z) = \left[1 - \hat{V}\hat{G}_0(z) \right]^{-1} \hat{V}. \quad (20)$$

When projected on shell, $\langle k | \hat{T}(k^2) | k \rangle$ becomes a 2×2 matrix which can then be diagonalized *via* a k -dependent passage matrix. The transformed 2×2 potential can

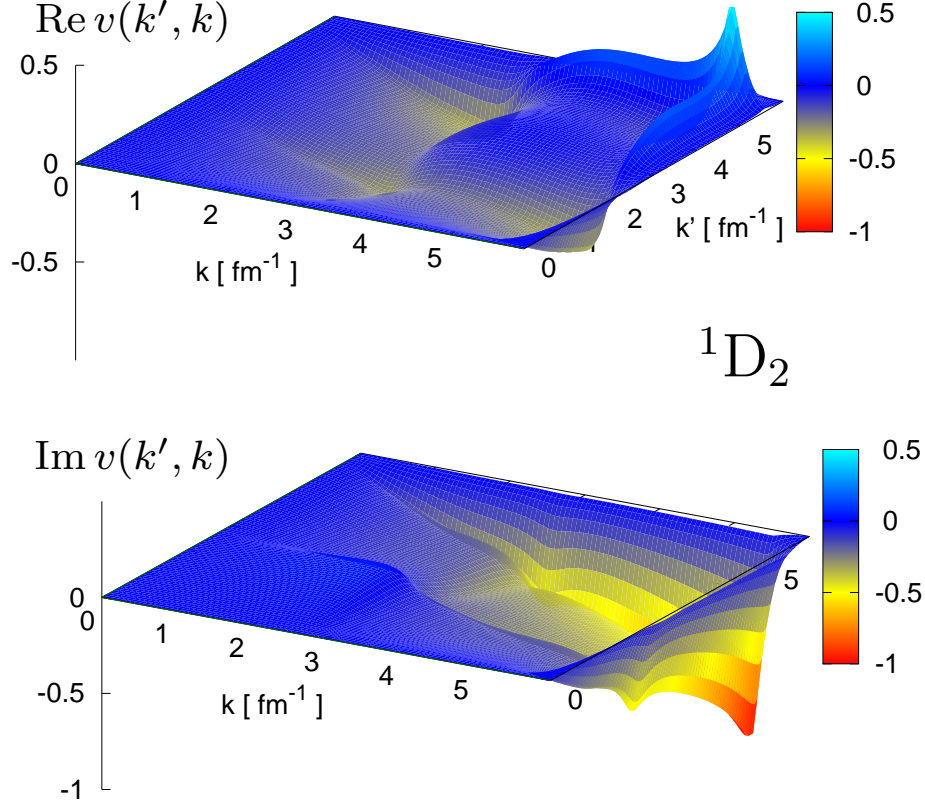


Fig. 12 Surface plot of the rank-1 energy-independent separable potential $v(k', k)$ in the 1D_2 channel, as function of the relative momentum. Upper and lower surfaces correspond to the real and imaginary components of the potential, respectively.

then be assumed diagonal with separable terms. In this way the problem gets reduced to the search of two separable solutions, one for each term in the diagonalized T matrix.

Appendix

T matrix for non-overlapping multi-rank separable potentials

Let us consider a non-overlapping rank- N potential defined as

$$\hat{V} = \sum_{i=1}^N |a_i\rangle \lambda_i \langle \tilde{a}_i|, \quad (\text{A-1})$$

where we impose

$$\langle \tilde{a}_i | a_j \rangle = 0, \quad \text{for } i \neq j. \quad (\text{A-2})$$

In the context of this study, a way to achieve this non-overlapping feature is by defining

$$\langle \tilde{a}_i | k \rangle = \Theta(k - k_{i-1}) \Theta(k_i - k) \tilde{h}_i(k) , \quad (\text{A-3a})$$

$$\langle k | a_i \rangle = \Theta(k - k_{i-1}) \Theta(k_i - k) h_i(k) , \quad (\text{A-3b})$$

with $k_1 < k_2 < \dots < k_N$. Here $h_i(k)$ and $\tilde{h}_i(k)$ are functions on the domain $[k_{i-1}, k_i]$. The whole domain in k is reconstructed with the union of N non-overlapping intervals, namely

$$[0, \infty) = [k_0, k_1) \cup [k_1, k_2) \dots \cup [k_{N-1}, k_N) , \quad (\text{A-4})$$

where $k_0 \equiv 0$. Being the free propagator $\hat{G}_0(z)$ diagonal in momentum space, $\hat{G}_0(z) = 1/(z - \hat{p}^2)$, then

$$\langle \tilde{a}_i | \hat{G}_0(z) | a_j \rangle = \delta_{ij} \langle \tilde{a}_i | \hat{G}_0(z) | a_i \rangle . \quad (\text{A-5})$$

Let us now consider the Lippmann-Schwinger integral equation for the scattering \hat{T} matrix

$$\hat{T}(z) = \hat{V} + \hat{V} \hat{G}_0(z) \hat{T}(z) . \quad (\text{A-6})$$

Replacing \hat{V} from Eq. (A-1) and factorizing by \hat{T} on the left we get

$$\left[1 - \sum_i |\tilde{a}_i\rangle \lambda_i \langle a_i | \hat{G}_0(z) \right] \hat{T}(z) = \sum_j |\tilde{a}_j\rangle \lambda_j \langle a_j | . \quad (\text{A-7})$$

Hence

$$\hat{T}(z) = \left[1 - \sum_i |\tilde{a}_i\rangle \lambda_i \langle a_i | \hat{G}_0(z) \right]^{-1} \sum_j |\tilde{a}_j\rangle \lambda_j \langle a_j | . \quad (\text{A-8})$$

Considering that $\langle \tilde{a}_i | \hat{G}_0(z) | a_j \rangle = 0$, when $i \neq j$, then the above expression for \hat{T} yields

$$\hat{T}(z) = \sum_{i=1}^N \frac{|\tilde{a}_i\rangle \lambda_i \langle a_i |}{1 - \lambda_i \langle a_i | \hat{G}_0(z) | \tilde{a}_i \rangle} . \quad (\text{A-9})$$

Thus, the scattering matrix is also separable of rank- N .

When the above expression for \hat{T} is projected in momentum space as $\langle k | \dots | k \rangle$, with k in the i -th interval, then

$$\langle k | \hat{T}(z) | k \rangle \left[1 - \lambda_i \langle a_i | \hat{G}_0(z) | \tilde{a}_i \rangle \right] = \lambda_i \langle k | \tilde{a}_i \rangle \langle a_i | k \rangle . \quad (\text{A-10})$$

Therefore the equations for the form factors on each of the intervals get decoupled from one another.

Acknowledgements

The authors thank the partial support provided by the supercomputing infrastructure of the NLHPC (ECM-02): Powered@NLHPC. N.A.A. acknowledges funding under doctoral fellowship ANID-Subdirección de Capital Humano/Doctorado

Nacional/2019-21191174. H.F.A. is grateful for the hospitality received at CEA-DAM, Bruyères-le-Châtel, where part of this work was done.

References

- [1] H. Yukawa. On the Interaction of Elementary Particles. I. *Proceedings of the Physico-Mathematical Society of Japan. 3rd Series*, 17:48–57, 1935.
- [2] R. B. Wiringa, V. G. J. Stoks, and R. Schiavilla. Accurate nucleon-nucleon potential with charge-independence breaking. *Phys. Rev. C*, 51(1):38–51, Jan 1995.
- [3] M. Lacombe, B. Loiseau, J. M. Richard, R. Vinh Mau, J. Côté, P. Pirès, and R. de Tourreil. Parametrization of the Paris N - N potential. *Phys. Rev. C*, 21:861–873, Mar 1980.
- [4] V. G. J. Stoks, R. A. M. Klomp, C. P. F. Terheggen, and J. J. de Swart. Construction of high-quality NN potential models. *Phys. Rev. C*, 49:2950–2962, Jun 1994.
- [5] Steven Weinberg. Nuclear forces from chiral lagrangians. *Physics Letters B*, 251(2):288–292, 1990.
- [6] Epelbaum, E., Krebs, H., and Meißner, U. -G. Improved chiral nucleon-nucleon potential up to next-to-next-to-next-to-leading order. *Eur. Phys. J. A*, 51(5):53, 2015.
- [7] D. R. Entem and R. Machleidt. Accurate charge-dependent nucleon-nucleon potential at fourth order of chiral perturbation theory. *Phys. Rev. C*, 68:041001, Oct 2003.
- [8] J. W. Holt, N. Kaiser, and W. Weise. Density-dependent effective nucleon-nucleon interaction from chiral three-nucleon forces. *Phys. Rev. C*, 81(2):024002, February 2010.
- [9] K. Hebeler and A. Schwenk. Chiral three-nucleon forces and neutron matter. *Phys. Rev. C*, 82(1):014314, July 2010.
- [10] M. Piarulli, L. Girlanda, R. Schiavilla, R. Navarro Pérez, J. E. Amaro, and E. Ruiz Arriola. Minimally nonlocal nucleon-nucleon potentials with chiral two-pion exchange including Δ resonances. *Phys. Rev. C*, 91:024003, Feb 2015.
- [11] David Rodriguez Entem, Ruprecht Machleidt, and Yevgen Nosyk. Nucleon-Nucleon Scattering Up to N5LO in Chiral Effective Field Theory. *Frontiers in Physics*, 8, 2020.

- [12] K. O. Eyser, R. Machleidt, and W. Scobel. Modelling nucleon-nucleon scattering above 1 GeV. *The European Physical Journal A - Hadrons and Nuclei*, pages 105,117, 2004.
- [13] A. Funk, H. V. von Geramb, and K. A. Amos. Nucleon-nucleon optical model for energies up to 3 GeV. *Phys. Rev. C*, 64:054003, Oct 2001.
- [14] H. F. Arellano and H. V. von Geramb. Extension of the full-folding optical model for nucleon-nucleus scattering with applications up to 1.5 GeV. *Phys. Rev. C*, 66:024602, Aug 2002.
- [15] Yoshio Yamaguchi. Two-Nucleon Problem When the Potential Is Nonlocal but Separable. I. *Phys. Rev.*, 95:1628–1634, Sep 1954.
- [16] M. Bolsterli and J. MacKenzie. Determination of separable potential from phase shift. *Physics*, 2:141–149, Nov 1965.
- [17] Frank Tabakin. Inverse scattering problem for separable potentials. *Phys. Rev.*, 177:1443–1451, Jan 1969.
- [18] N. H. Kwong and H. S. Köhler. Separable NN potentials from inverse scattering for nuclear matter studies. *Phys. Rev. C*, 55:1650–1664, Apr 1997.
- [19] J. Haidenbauer and W. Plessas. Separable representation of the paris nucleon-nucleon potential. *Phys. Rev. C*, 30:1822–1839, Dec 1984.
- [20] S.G. Bondarenko, V.V. Burov, and E.P. Rogochaya. Relativistic complex separable potential for describing the neutron-proton system in s13-d13 partial-wave state. *Nuclear Physics B - Proceedings Supplements*, 219-220:126–129, 2011. The Proceedings of the 5th Joint International Hadron Structure '11 Conference.
- [21] N. A. Khokhlov and L. I. Studenikina. Energy-independent complex 1S_0 NN potential from the Marchenko equation. *Phys. Rev. C*, 104:014001, Jul 2021.
- [22] H. Kamada and W. Glöckle. Momentum Transformation Connecting a NN Potential in the Nonrelativistic and Relativistic Two-Nucleon Schrödinger Equation. *Phys. Rev. Lett.*, 80:2547–2549, Mar 1998.
- [23] H. Kamada and W. Glöckle. Realistic two-nucleon potentials for the relativistic two-nucleon Schrödinger equation. *Physics Letters B*, 655(3):119 – 125, 2007.
- [24] R. Machleidt. High-precision, charge-dependent Bonn nucleon-nucleon potential. *Phys. Rev. C*, 63:024001, Jan 2001.
- [25] Richard A. Arndt and L. David Roper. Parametrizing the nucleon-nucleon scattering matrix above the inelastic threshold. *Phys. Rev. D*, 25:2011–2012, Apr 1982.

- [26] Richard A. Arndt, L. David Roper, Ronald A. Bryan, Robert B. Clark, Bruce J. VerWest, and Peter Signell. Nucleon-nucleon partial-wave analysis to 1 GeV. *Phys. Rev. D*, 28:97–122, Jul 1983.
- [27] R.J. Furnstahl. The renormalization group in nuclear physics. *Nuclear Physics B - Proceedings Supplements*, 228:139–175, 2012. “Physics at all scales: The Renormalization Group” Proceedings of the 49th Internationale Universitätswochen für Theoretische Physik.
- [28] R. A. Arndt, W. J. Briscoe, I. I. Strakovsky, and R. L. Workman. Updated analysis of NN elastic scattering to 3 GeV. *Phys. Rev. C*, 76:025209, Aug 2007.
- [29] W. Briscoe. *The George Washington University - Data Analysis Center*, 1994 (accessed March 20, 2020). Phase-shift data accessible for download from <http://gwdac.phys.gwu.edu/>.
- [30] R. Brockmann and R. Machleidt. Relativistic nuclear structure. I. Nuclear matter. *Phys. Rev. C*, 42:1965–1980, Nov 1990.
- [31] Richard H. Thompson. Three-Dimensional Bethe-Salpeter Equation Applied to the Nucleon-Nucleon Interaction. *Phys. Rev. D*, 1:110–117, Jan 1970.